

## MIT Open Access Articles

*Mach 3.5 Compression Corner  
Control Using Microvortex Generators*

The MIT Faculty has made this article openly available. **Please share** how this access benefits you. Your story matters.

**Citation:** Daniel C. Gochenaur, Rhys D. Williams, Kshitij Sabnis, and Holger Babinsky, "Mach 3.5 Compression Corner Control Using Microvortex Generators," AIAAJ, Vol. 62, No. 5 (2024), pp. 1731-1743 doi: doi/abs/10.2514/1.J063469

**As Published:** 10.2514/1.j063469

**Publisher:** American Institute of Aeronautics and Astronautics (AIAA)

**Persistent URL:** <https://hdl.handle.net/1721.1/153917>

**Version:** Author's final manuscript: final author's manuscript post peer review, without publisher's formatting or copy editing

**Terms of use:** Creative Commons Attribution-Noncommercial-ShareAlike



# Mach 3.5 Compression Corner Control Using Micro-Vortex Generators

Daniel C. Gochenaur\*

*Massachusetts Institute of Technology, Cambridge, MA, 02139*

Rhys D. Williams†

*University of Cambridge, Cambridge, CB2 1PZ, UK*

Kshitij Sabnis‡

*Queen Mary University of London, London, E1 4NS, UK*

Holger Babinsky§

*University of Cambridge, Cambridge, CB2 1PZ, UK*

An experimental investigation has been performed to examine the effect of vortex generators (VGs) on a compression corner flow separation. Experiments are conducted at Mach 3.5 along a  $23^\circ$  compression corner with turbulent inflow boundary-layer and Reynolds number  $27 \times 10^4$  based on the 6.2-mm boundary-layer thickness. Micro-ramp, standard ramped-vane, and inverted ramped-vane VGs all cause the separation line to ripple and become more three-dimensional, but none eliminate it altogether. Vane-type VGs produce a stronger control effect than micro-ramps. Inverted vanes tend to generate large areas of near-wall low-momentum flow that locally increase separation length, making standard vane configurations more effective at reducing separation size. Velocimetry measurements show that the VG-induced vortices remain coherent and capable of exchanging momentum within the boundary-layer, even downstream of the interaction. Enhanced flow three-dimensionality causes an intensification of areas of increased and decreased momentum downstream of reattachment, resulting in significant flow distortion. Increased near-wall turbulent fluctuations are observed upstream of the interaction in areas where separation length is reduced. These findings are used to propose a mechanism of VG control highlighting the role of VGs to enhance mixing in the separated shear layer, leading to earlier reattachment and an overall reduction in separation length.

## I. Nomenclature

---

\*Graduate Student, Department of Aeronautics and Astronautics, AIAA Student Member, dgochena@mit.edu (Corresponding Author).

†Graduate Student, Department of Engineering, AIAA Student Member.

‡Lecturer in Aerospace Engineering, School of Engineering and Materials Science, AIAA Member.

§Professor of Aerodynamics, Department of Engineering, AIAA Fellow.

An earlier version of this manuscript was presented on January 24, 2023 at AIAA SciTech 2023 Forum in National Harbor, MD. Paper number AIAA 2023-0852.



$\alpha$	=	compression corner deflection angle
$\delta$	=	boundary-layer thickness
$\delta_i^*$	=	incompressible boundary-layer displacement thickness
$h$	=	vortex generator device height
$H_i$	=	incompressible boundary-layer shape factor
$L_{sep}$	=	separation length
$M_\infty$	=	free stream Mach number
$P$	=	static pressure
$P_0$	=	stagnation pressure
$\theta_i$	=	incompressible boundary-layer momentum thickness
$\theta_S$	=	flow separation deflection angle
$u_\infty$	=	free stream velocity
$u_{rms}$	=	streamwise velocity root-mean-square
$x_{VG}$	=	vortex generator streamwise placement location
$x$	=	streamwise coordinate
$y$	=	floor-normal coordinate
$z$	=	spanwise coordinate

## II. Introduction

IN the inlets of supersonic aircraft, shock wave-boundary-layer interactions (SBLIs) are inevitable and can have significant detrimental impacts on the overall performance of the propulsion system. Within an SBLI, strong adverse pressure gradients (APGs) can cause the boundary-layer to separate, leading to increased stagnation pressure losses, large-scale flow unsteadiness, and even inlet unstart in severe cases [1]. As such, there is significant interest in identifying flow control techniques to reduce the size of flow separation and alter the behavior of the SBLI. The most common (and perhaps, the most effective) method is boundary-layer bleed. Boundary-layer bleed involves the removal of a portion of the low-momentum near-wall flow, thereby making the boundary-layer more resistant to an ensuing APG [2]. Although effective, this approach requires that the inlet is made larger to account for the lost mass-flow to the engine, ultimately elevating the overall drag penalty of the propulsion system [3]. Plasma actuators and air-jet vortex generators (AJVGs) are alternative control methods that have shown some success when used to control shock-induced flow separations [4, 5]. However, both devices require an energy input (and in the case of AJVGs, internal ducting to move the high-velocity air) which increases system complexity and makes them less useful for many practical applications.

Mechanical vortex generators (VGs) are an alternative passive control method that have shown some promise [6].

VGs control a separation by inducing streamwise vortices in the boundary-layer upstream of the interaction region. The streamwise vortices are thought to alter the boundary-layer by redistributing regions of higher and lower momentum flow. In doing so, higher momentum is brought closer to the wall in regions of vortex "downwash", thereby energizing portions of the near-wall flow as illustrated in Fig. 1. There are corresponding regions of vortex "upwash" with low-momentum flow, however these regions tend to move away from the surface as the vortices progress downstream [7]. The overall resulting increase in near-wall momentum therefore reduces or eliminates any downstream flow separation. The devices can be broadly categorized as either "ramp-type" or "vane-type" VGs based on their geometry. Ramp-types have a comparatively large planform area with a triangular side profile, while vane-types tend to have a thin planform area with a rectangular or triangular side profile. Mechanical VGs have been successfully employed in many subsonic situations, where they typically have a height on the order of one boundary-layer thicknesses [8]. However, at high speeds these devices tend to incur significant parasitic drag [9]. As such, in the supersonic regime an alternative approach is adopted wherein micro-VGs with height much smaller than one boundary-layer thickness are typically used. With this approach, momentum is redistributed within the boundary-layer, rather than transferred from the outer flow to the boundary-layer. In contrast to their subsonic performance, the use of VGs upstream of SBLIs has not consistently demonstrated a significant reduction of shock-induced separation [6]. Several studies have shown that VGs may provide some benefit when positioned upstream of normal [10] or oblique shock reflection [7] SBLIs. However, less is known of their performance when used to control separation along a compression corner, a canonical SBLI which is commonly encountered in inlet-type flow fields.

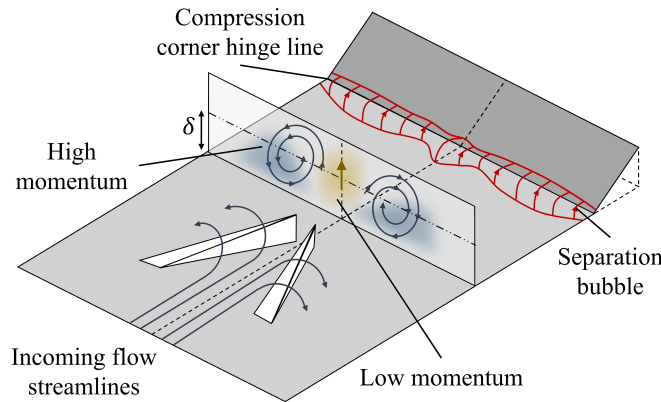


**Fig. 1 Schematic of ramped-vane vortex generators interacting with an incoming boundary-layer and subsequent effect on compression corner flow separation.**

In a 1970 study, Gartling [11] investigated the effect of vane-type VGs of various sizes and placement locations on a Mach 4.67, 35° compression corner flow separation. In general, Gartling [11] found that the VGs had little effect on the size of the separation. However, when the devices were placed sufficiently close to the interaction, significant spanwise separation shock corrugation was observed. Furthermore, Gartling reported that the VGs generated thin attached flow

channels through the interaction, although images of the flow field showing this result were not provided. Following Gartling's study, Barter and Dolling [12] investigated the effect of a staggered array of ramp-type VGs on a Mach 5,  $28^\circ$  compression corner SBLI. They observed a reduction in intensity of low-frequency unsteadiness, but the overall effect on the size of the separation was minor.

In 2012, Verma, *et al.* [13] investigated the effect of an array of ramp-type VGs at various locations upstream of a Mach 2,  $24^\circ$  compression corner SBLI. Verma, *et al.* found that the VGs caused the separation and reattachment streamlines to become highly corrugated, but with little change in the overall separation size. The authors also found that the VGs had a stronger effect when placed near the interaction at a distance of  $12.5\delta$  upstream of the hinge line compared with their performance when placed  $27.5\delta$  from the hinge line. A later study by Verma and Manisankar [14] examined the effect of device size and spacing within a vane-type VG array at the same test conditions as their 2012 study [13]. The authors found that altering inter-device spacing resulted in topological changes to the downstream separation, and that certain configurations could locally reduce separation extent by more than 50%. A similar study by Schreyer, *et al.* [15] investigated the effect of a staggered array of Anderson micro-ramps on a Mach 7.2,  $33^\circ$  compression corner flow separation. The authors observed that the separation length was locally increased in regions with a common upwards flow between vortices, and was locally decreased in regions with a common downwards flow [15].

In essence, the five studies mentioned above form a useful picture concerning our current understanding on the capabilities mechanical VGs to control a flow separation on supersonic compression corners. Nevertheless, a number of important questions remain. As most studies have focused on arrays of ramp-type rather than vane-type VGs, the best type of VG for compression corner control is still uncertain. In previous studies of other SBLIs, ramp-type VGs have been shown to be less effective than vane-types [16], but it remains to be established whether this is also the case along compression corners. Further, it is unknown how, or if, the device configuration affects its most effective location. Corrugation of the separation streamline and shock front have been observed, but it is unclear how these are linked and what they imply regarding the influence of the VGs on the SBLI. Similarly, it is not known whether the VG-induced vortices survive the SBLI, or if the APG causes them to burst or rapidly decay. Clarifying the vortex behavior would be especially useful for understanding the role of VGs in engine inlets where there are typically several successive SBLIs, all of which may require some level of control. Additionally, the survival or decay of VG-induced streamwise vortices is relevant for understanding the development of flow distortion after reattachment, which could affect the performance of downstream turbomachinery [17].

In order to answer these outstanding research questions, this study seeks to expand the current state of knowledge of the mechanisms by which streamwise vortices modify a supersonic compression corner SBLI, and provide insight on the effect of VG configuration and upstream location on flow separation size and shape. Various VG single device configurations (rather than an array) are studied to reveal the underlying flow physics. In addition, the flow field downstream of reattachment is surveyed to determine the post-interaction behavior of VG-induced vortices.

### III. Methodology

#### A. Wind Tunnel Setup

Experiments were conducted in the University of Cambridge supersonic blow-down wind tunnel facility. The test section has a rectangular cross section with a width of 114 mm and height of 172 mm. A symmetric, two-dimensional nozzle is used to generate a flow with a nominal free stream Mach number of 3.5 and a Reynolds number of  $27 \times 10^4$  based on the inflow boundary-layer thickness. The stagnation pressure is set to 931 kPa, fluctuating by a maximum of  $\pm 1\%$  during the run. The stagnation temperature is  $285 \text{ K} \pm 5 \text{ K}$ . This results in a nominal free stream velocity ( $u_\infty$ ) of 640 m/s. The inflow boundary-layer thickness ( $\delta$ ) on the tunnel floor is measured to be 6.2 mm at the tunnel centerline 25 mm upstream of the compression corner hinge line. An oblique shock wave is generated in the test section using a  $23^\circ$  full-span compression corner, shown in Fig. 2a. This deflection angle was selected such that its dimensionless interaction intensity (as defined by Souverein [18]) matches that of other recent compression corner studies conducted at Mach 2.5 [19, 20]. Furthermore, the predicted size of the separation according to the model proposed by Souverein [18] is sufficiently large that it would typically be thought to require control. Another advantage of the relatively high inflow Mach number is that the significant pressure rise across the resulting interaction allows for better visualization of small structures within the SBLI using pressure sensitive paint. The ramp surface is 150 mm in length (approximately  $24\delta$ ). This ensures that the trailing ramp edge is approximately  $20\delta$  downstream of reattachment and thus the expansion fan at the end of the ramp surface (Fig. 2b) does not affect the compression corner interaction at the focus of this study. A relief system is installed above the ramp surface as shown in Fig. 2b to increase the vertical space in the aft section of the tunnel and prevent unstart. For cases with VG control, the VGs are placed between the end of the nozzle and hinge line at a desired streamwise location ( $x_{VG}$ ) relative to the compression corner hinge line. In all cases, the devices are placed such that their centerline is coincident with the tunnel centerline.

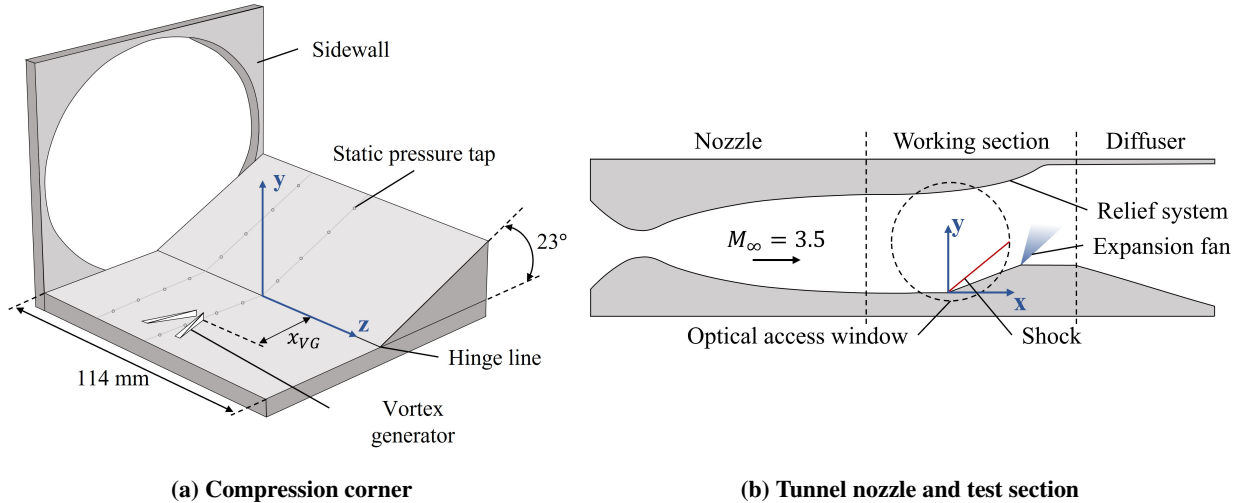


**Fig. 2** Diagrams showing wind tunnel setup.

## B. Vortex Generator Design

A micro-ramp of the type studied by Anderson, *et al.* [21] as well as "standard" and "inverted" ramped-vane (RV) devices based on those proposed by Lee, *et al.* [16] have been tested. The dimensions of each VG are shown in Fig. 3. The devices have height ( $h$ ) of  $0.45\delta$ , based on recommendations from the survey by Lee and Loth [22]. The devices are 3D printed using opaque PolyJet resin.

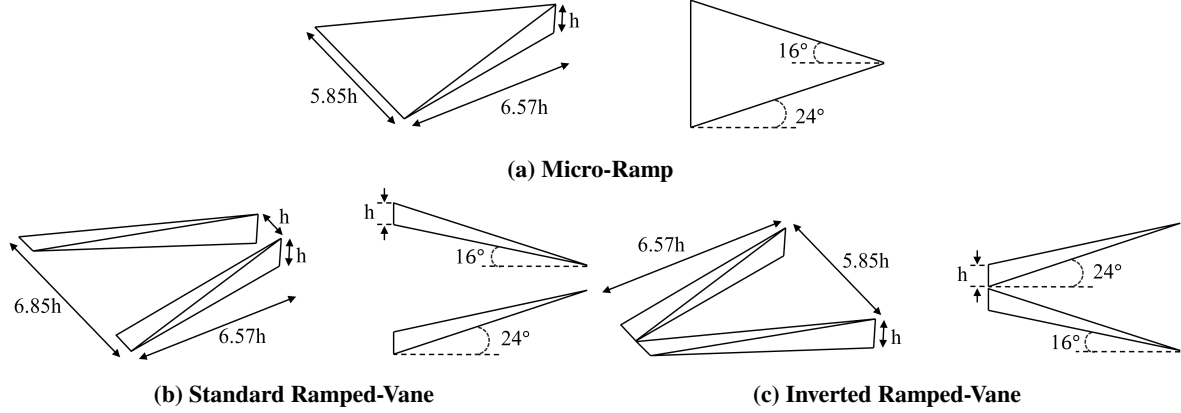


**Fig. 3 Design parametrization of tested micro-VGs.**

For this investigation, single device VGs are positioned reasonably far from the sidewalls to minimize any effects due to the finite span of the tunnel. The micro-ramps and standard ramped-vanes induce "common flow up" (CFU) counter-rotating vortices with an upwards velocity on the device centerline, while the inverted ramped-vanes induce "common flow down" (CFD) vortices with a downwards velocity on the device centerline, as shown in Fig. 4.

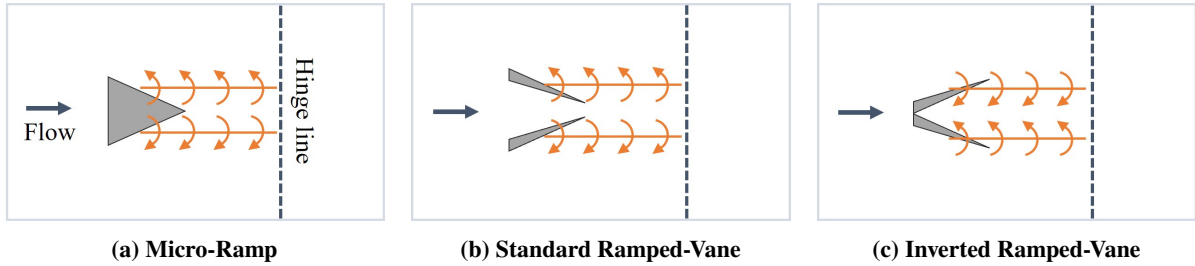


**Fig. 4 Schematic of device counter-rotating vortex direction. Micro-ramps and standard ramped-vanes generate CFU vortices, while inverted ramped-vanes generate CFD vortices.**

## C. Measurement Techniques

The flow field is visualized using dual-mirror z-type schlieren photography with a horizontal knife edge to observe span-averaged wall-normal density gradients. A 4 W LED is used as a light source. Videos are recorded using a Photron Fastcam Nova S6 camera at a frame rate of 1000 frames per second and shutter speed of  $11 \mu s$ . Presented schlieren images are time-averaged across 500 frames at minimum.

Surface oil-flow visualization is used to obtain time-averaged skin friction lines on the tunnel floor. The oil mixture consists of paraffin, powdered titanium dioxide, oleic acid, and lubricating oil. Before a run, the mixture is painted onto the tunnel floor around the compression corner hinge line. Videos are recorded during the run using a Nikon D850 camera with a tilt-shift lens to observe streamline development. Representative oil-flow images are then selected from a video frame during fully established flow. The frames are converted to grey-scale and filtered using contrast-limited adaptive histogram equalization to improve contrast. The images are then corrected for perspective distortion to generate a view of the oil-flow visualization as if it was observed normal to the tunnel surface. Lines of separation and reattachment are identified from the filtered and perspective-corrected video frames. Using this correction technique and camera setup, the spatial resolution is approximately 25 pixels per mm. The uncertainty in the determination of separation and reattachment streamline locations is  $0.2\delta$  as suggested by Squire [23], or about 1.2 mm for this study.

Pressure sensitive paint (PSP) is used to visualize the surface pressure distribution of the tunnel floor. The intensity of light emission from PSP is related to the pressure when the paint is exposed to ultraviolet illumination. The PSP field is illuminated using a UV light source with wavelength of 400 nm. Images are captured using a Nikon D850 camera with a 550 nm long-pass filter. During a tunnel run, a "wind-on" image of the PSP field is taken after the flow is established. A "wind-off" reference image of the same field is then taken immediately after tunnel shutdown such that the surface temperature and paint response characteristics best match those for the wind-on image. In situ calibration is performed using 16 pressure tappings in the tunnel floor to ascertain the Stern-Volmer coefficients [24] from the ratio of the red-channel pixel intensities of the wind-off and wind-on images. These tappings are connected to a NetScanner 9116 differential pressure transducer via neoprene tubes. The NetScanner 9116 has a total error of  $\pm 0.5\%$  for stagnation pressure ( $P_0$ ) normalized measurements from tappings. Noise is reduced by applying a 10 by 10 pixel Gaussian filter to the pixel intensities. A comparison between the values recorded from the pressure tappings and the calibrated PSP data gives a maximum error of  $\pm 5\%$  for the PSP measurement. As with the oil flow visualizations, PSP images are corrected for distortion using a projective transformation method on the tunnel floor and ramp surfaces. This method yields a PSP image resolution of 50 pixels per mm.

Streamwise and floor-normal velocities are recorded using two-component laser Doppler velocimetry (LDV). The flow is seeded in the settling chamber using paraffin droplets with average diameter of approximately  $0.5\ \mu\text{m}$  [25]. The emitter is a two-component Powersight diode-pumped solid state laser system manufactured by TSI. A TSI RV 70 optical receiver with FSA 4000 digital processor captures light scattered by seeding particles during the run and identifies the dominant scatter frequency difference. The laser and receiver are mounted on a three-axis traverse system that enables velocity measurements across a line of points during a tunnel run. Uncertainty in the probe volume alignment is approximately 0.5 mm in  $x$ , 0.005 mm in  $y$ , and 0.1 mm in  $z$ . There is a contribution to the measurement uncertainty of the flow velocities due to slight misalignment of the laser optics head relative to the tunnel floor, estimated to be 0.3% in the streamwise direction and 10% in the floor-normal direction. When LDV data is processed, data is stored in bins

that are categorized based on the location of the probe volume during a traverse. Most bins contain at least 2000 data points, for which a mean velocity error of about 2% is obtained assuming a maximum turbulent intensity of 10% [26]. Uncertainty is typically larger near the wall or within separated shear layers where particle counts are low. Measured velocities are fitted to theoretical turbulent boundary-layer profiles following the approach of Colliss [27], from which the integral boundary-layer parameters are identified. Accounting for uncertainty propagation, the error in normalized streamwise turbulent intensity values is conservatively estimated at  $\pm 5\%$ .

## IV. Results and Discussion

### A. Baseline Flow

The incompressible baseline boundary-layer parameters measured using LDV at the tunnel centerline 25 mm ( $4\delta$ ) upstream of the compression corner hinge line are listed in Table 1. Incompressible (rather than compressible) parameters are provided because they can be measured directly and are less dependent on Mach number, making them more useful for comparison at different flow velocities as discussed by Détery in [1].

**Table 1** Boundary-layer parameters, measured along the tunnel centerline 25 mm ( $4\delta$ ) upstream of the compression corner hinge line.

$\delta$ (mm)	$\delta_i^*$ (mm)	$\theta_i$ (mm)	$H_i$
6.20	0.864	0.659	1.31

A time-averaged schlieren image of the baseline flow is presented in Fig. 5. The separation shock originates upstream of the hinge line, indicating the presence of a separation bubble. The reattachment shock is difficult to identify, as it is smeared in nature, partially hidden by the turbulent boundary-layer on the ramp surface, and likely merges with the separation shock within this boundary-layer. The resultant far-field shock is indicated in the figure. The angle of the far-field shock is consistent with the  $38^\circ$  inviscid shock angle for a  $23^\circ$  flow deflection at Mach 3.5. The existence of "interface waves" stemming from the junction between the nozzle and test section is also observed. The strength of their

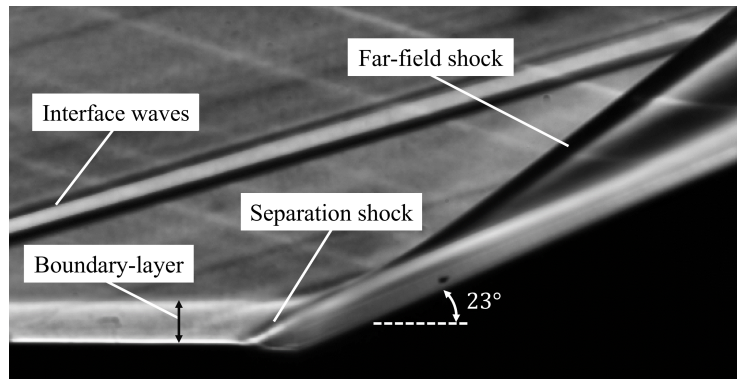


**Fig. 5** Time-averaged schlieren image of baseline flow.

appearance in Fig. 5 is partially an artifact of the enhanced contrast applied to the image to improve visualization of the boundary-layer. The angle of these waves indicates that they are Mach waves, suggesting that they are weak and do not significantly alter the flow field.

The baseline flow separation on the tunnel floor is visualized across the entire tunnel span using oil-flow in Fig. 6a. The area of separated flow is highlighted in red. In general, the separation appears highly two-dimensional, with sidewall effects limited to approximately 18% of the total span proximate to each sidewall. The oil-flow visualization also shows streaks downstream of reattachment that may indicate the presence of Görtler vortices, a boundary-layer instability generally associated with wall curvature [28]. The two-dimensional nature of the interaction near the centerline is also highlighted by the wall pressure field in Fig. 6b. A pressure trace extracted along the tunnel centerline shown in Fig. 7 appears to converge to the inviscid values both upstream and downstream of the interaction. There is a clear separation pressure rise and a visible pressure plateau. The reattachment pressure rise is also visible, but is highly smeared.

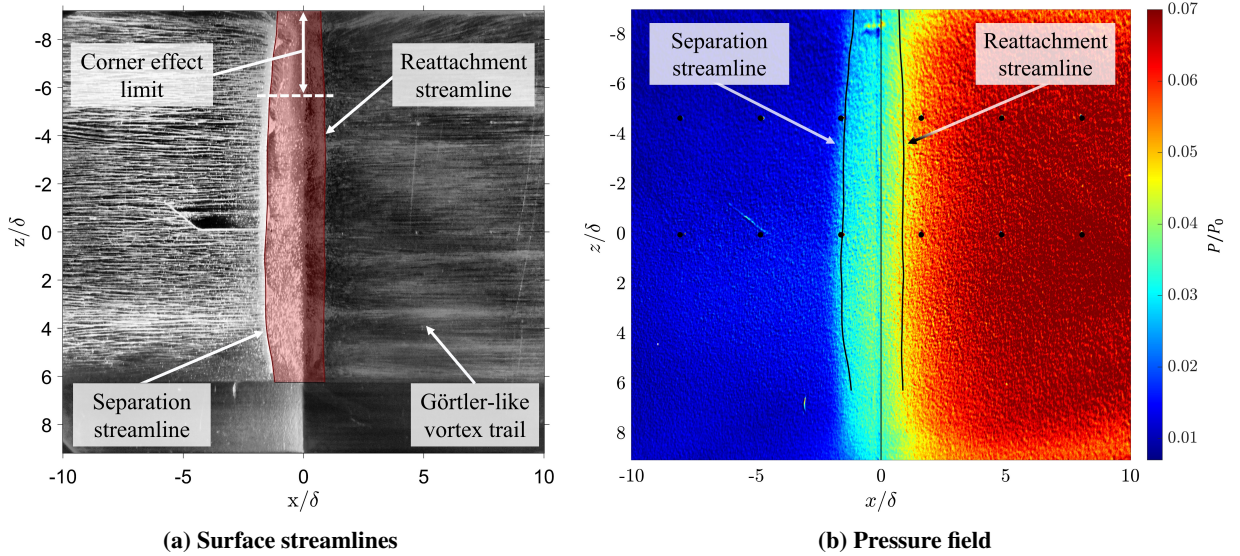


**Fig. 6 Full-span baseline surface oil-flow streamline visualization with separated area marked in red and baseline pressure field at the tunnel floor with overlaid lines of separation and reattachment from oil-flow. Pressure tapping locations are indicated with black dots.**

## B. Characterization of Unperturbed VG Flow Fields

Before investigating the effect of the various VG configurations on the compression corner flow separation, the vortex development and resulting momentum exchange upstream of the SBLI is examined. Data is presented in the form of relative velocity contour plots, where the baseline uncontrolled values are subtracted from the velocity components with VG control measured at the same locations. To generate the contours, LDV traverses are performed at spanwise locations of  $0.0\delta$ ,  $0.5\delta$ ,  $1.0\delta$ ,  $2.0\delta$ , and  $3.0\delta$  from the device centerline. Linear interpolation is used to fill the velocity data between traverses. To reduce the number of required LDV runs, spanwise symmetry is assumed and the data is



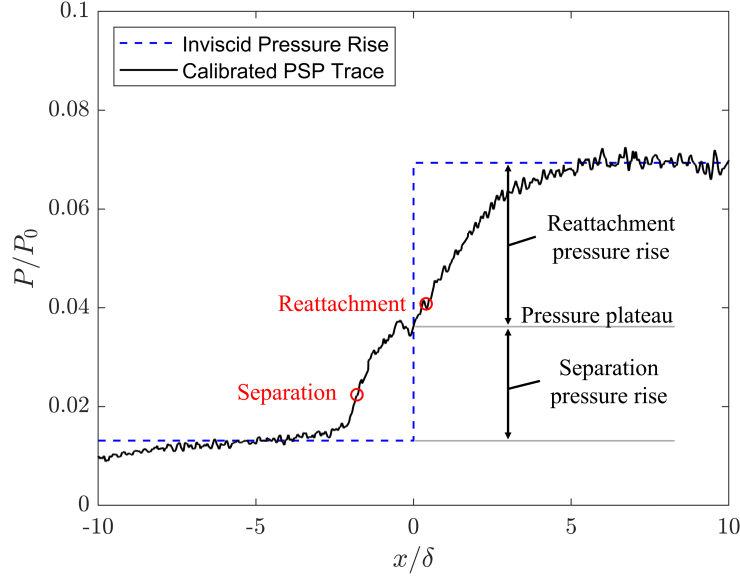


**Fig. 7** Baseline pressure trace through tunnel centerline using PSP (Fig. 6b). Separation and reattachment locations determined from oil-flow (Fig. 6a).

mirrored across the device centerline. The velocity contours are cut-off near the wall when the data rate drops below 800 seeding particles per second, which typically occurs within 1 mm (approximately  $0.16\delta$ ) of the floor. Measurement planes are recorded at least  $4\delta$  upstream of the compression corner hinge line so that the SBLI does not affect the results.

Contour plots of the relative vertical velocity at locations  $3\delta$ ,  $7\delta$ , and  $11\delta$  downstream of the micro-ramp, standard ramped-vane, and inverted ramped-vane are shown in Fig. 8. The spanwise vortex core positions are determined from the footprints seen in the surface oil-flow visualizations presented later in this section, while the wall-normal positions are estimated from the vertical center of the areas of positive and negative vertical velocity. The resulting approximate vortex core locations are indicated with magenta circles. Note that the LDV system can only measure velocity components in the streamwise and floor-normal directions, and as such vortex strength cannot be determined directly.

As expected, Fig. 8 shows that the micro-ramp and standard ramped-vanes (the CFU devices) induce flow fields with an upwards velocity along the device centerline, while the inverted ramped-vanes (the CFD device) generate a flow field with a downward velocity along the centerline. In turn, the vortex cores of the CFU devices drift marginally upward with streamwise distance, while the inverted ramped vane cores remain near the wall. Furthermore, the CFU device vortex cores drift marginally closer to the device centerline over distance, while those of the inverted ramped-vanes appear to remain apart. Such results are consistent with expected trajectories due to velocities induced by image vortices with the wall as a plane of symmetry [29].

It is observed that the standard ramped-vanes generate comparatively larger regions of upwards and downwards velocity than the micro-ramp. For both devices, the relative upwash and downwash becomes weaker with streamwise

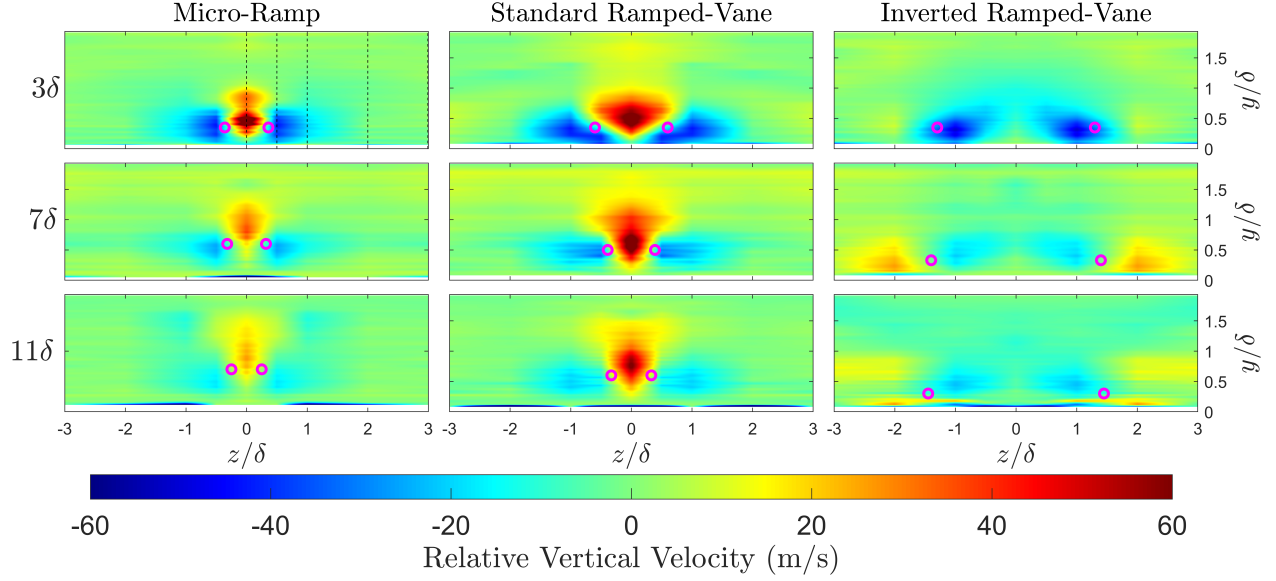


**Fig. 8** Relative wall-normal velocity contours at various measurement locations downstream of VGs. Approximate vortex core locations are indicated with magenta circles. Black dashed lines in upper left image indicate LDV traverse locations.

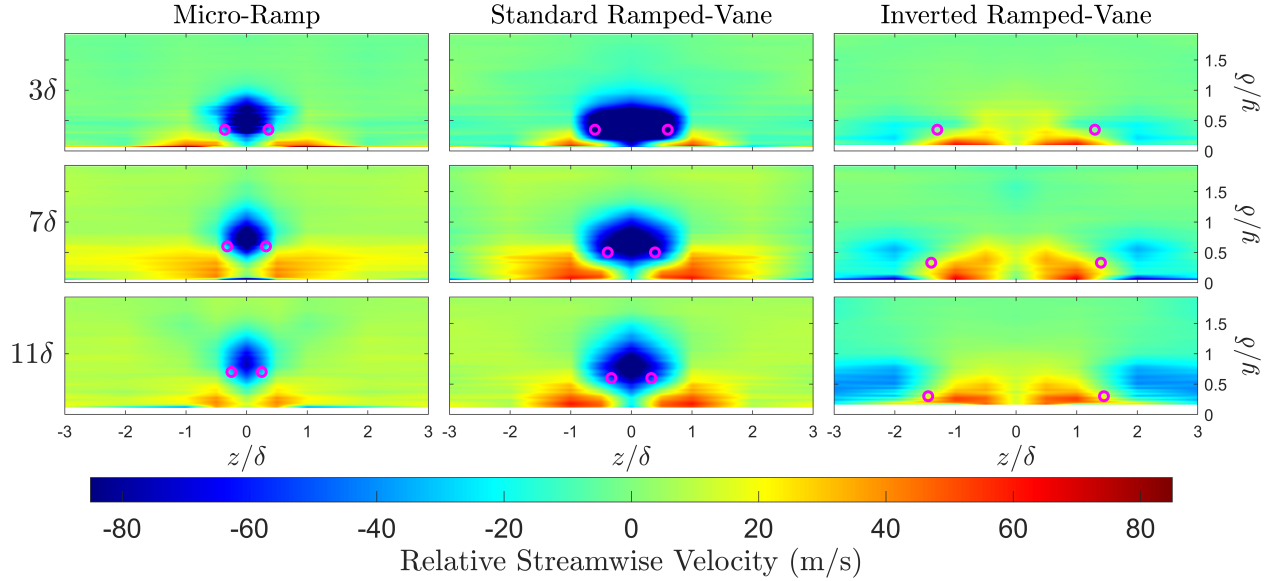


**Fig. 9** Relative streamwise velocity contours at various measurement locations downstream of VGs. Approximate vortex core locations are indicated with magenta circles.

distance, suggesting that the vortices are slowly decaying. The inverted ramped-vanes generate regions of upwash and downwash that appear weaker than those of the micro-ramp and standard ramped-vanes.

The corresponding streamwise relative velocity plots at the same downstream measurement locations are shown in Fig. 9. The micro-ramp and standard ramped-vanes generate a low-momentum "bubble" in the upwash region, as lower momentum from the near-wall flow is swept upward within the boundary-layer. The opposite effect occurs in the

downwash regions, where regions of increased momentum are observed near the wall. Similarly, the inverted ramped-vanes increase momentum in the downwash region on the device centerline, but also generate large low-momentum regions on the device shoulders (the spanwise sections  $1.5\delta$  to  $3\delta$  from either side of the centerline).

### C. Compression Corner Cases with VG Control

Time-averaged schlieren images with the VGs placed  $4\delta$  upstream of the compression corner hinge line are shown in Figure 10. The VGs cause a flow deflection leading to the formation of weak shock waves upstream of the main interaction. As the compression generated by these shocks is believed to be small, it is unlikely that they have a significant effect on the downstream flow.

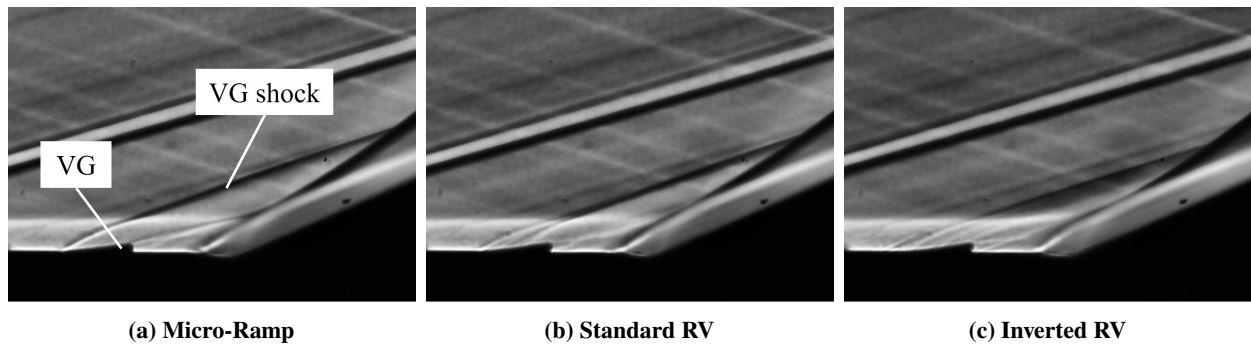


**Fig. 10 Time-averaged schlieren flow field visualization images with VGs placed  $4\delta$  upstream of the hinge line.**

Figure 11 shows a full-span surface oil-flow visualization for a representative test of the standard ramped-vanes. For ease of comparison between test cases, oil-flow visualizations from the nine test cases (three VGs at three placement locations) are presented in a matrix layout in Fig. 12. The yellow dashed line in Fig. 11 indicates the areas displayed in these images. This area extends  $7.1\delta$  upstream and downstream of the hinge line, and  $6.5\delta$  to either side of the tunnel centerline. Figure 11 shows that the corner separation has remained similar in size (compared to the baseline results in Fig. 6a) with the VGs installed. As such, sidewall effects are unlikely to significantly affect analysis on the influence of the VGs on the separation near the tunnel centerline.

All images in Fig. 12 exhibit dark regions exist downstream of the devices where the oil has been transported away by high wall shear stresses. The high wall-shear areas are caused by the streamwise vortices and are typically visible both upstream and downstream of the hinge line, indicating that the vortices affect the flow field on both sides of the interaction. Similarly, smaller areas of oil accumulation corresponding to low wall-shear are also observed downstream of the VGs in the upwash regions of each device.

Figure 12 also shows that all examined VG configurations and positions are capable of locally reducing the separation length relative to the baseline (shown in cyan) in an area directly downstream of the devices, regardless of device location. The micro-ramps (Fig. 12a, 12d, & 12g) tend to have the greatest effect near the device centerline. The

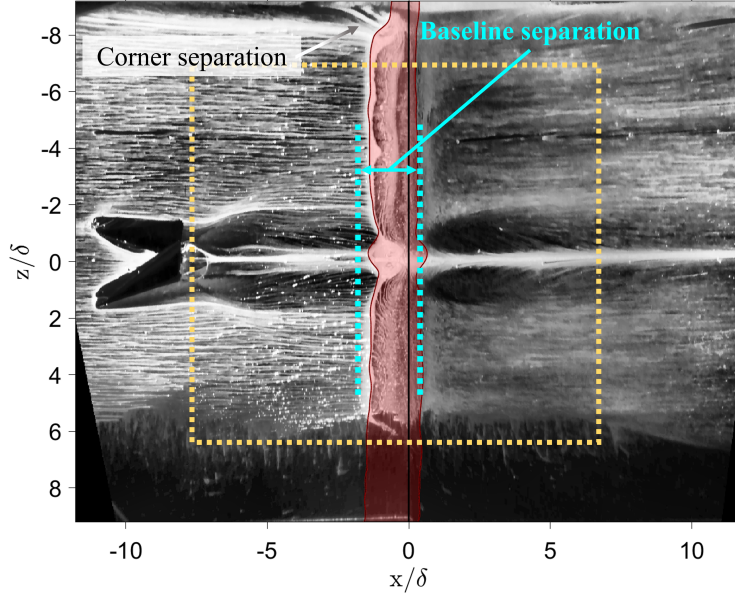


**Fig. 11 Full-span surface oil-flow visualization image for representative standard ramped-vanes control case with  $x_{VG} = 8\delta$ . The yellow dashed line indicates the areas displayed in Fig. 12.**

standard ramped-vane tests (Fig. 12b, 12e, & 12h) show a small region of increased separation along the centerline (in the upwash region). This "bulge" does not extend beyond the uncontrolled baseline, but it becomes less well defined as the devices are placed farther upstream. The inverted ramped-vanes (Fig. 12c, 12f, & 12i) tend to cause a local increase in separation size in the low-momentum regions on the device shoulders. These regions surround an area of local separation length reduction near the device centerline. This area of reduced separation length covers a larger spanwise extent when the inverted ramped-vanes are placed  $15\delta$  from the hinge line. The regions of high-wall shear downstream of reattachment also become larger when the device is placed farther from the hinge line.

Figure 13 presents the minimum ( $L_{sep,min}$ ) and maximum ( $L_{sep,max}$ ) separation lengths observed for the various VG configuration and location combinations. The figures are generated using the separation length definitions provided in Fig. 14. The micro-ramp and standard ramped-vanes (the CFU devices) show similar separation length variation with location. Both devices become less effective as they are placed farther upstream because the vortices weaken and lift away from the surface as they progress downstream, reducing the amount of near-wall high momentum flow (Fig. 9). Across the tested placement locations,  $L_{sep,min}$  of the standard ramped-vanes was 18% smaller than for the micro-ramp, confirming that standard ramped-vanes are more effective than micro-ramps at reducing separation length in compression corner SBLIs.

The locally increased separation length on the shoulders of the inverted ramped-vanes provides a striking example that VGs can have a locally negative influence on the separation. In contrast to the standard ramped-vanes where the generated low-momentum zone is strong but surrounded by regions of relatively high-momentum, the low-momentum areas of the inverted ramped-vanes are left unconfined. As a result, the low-momentum areas become larger and spread



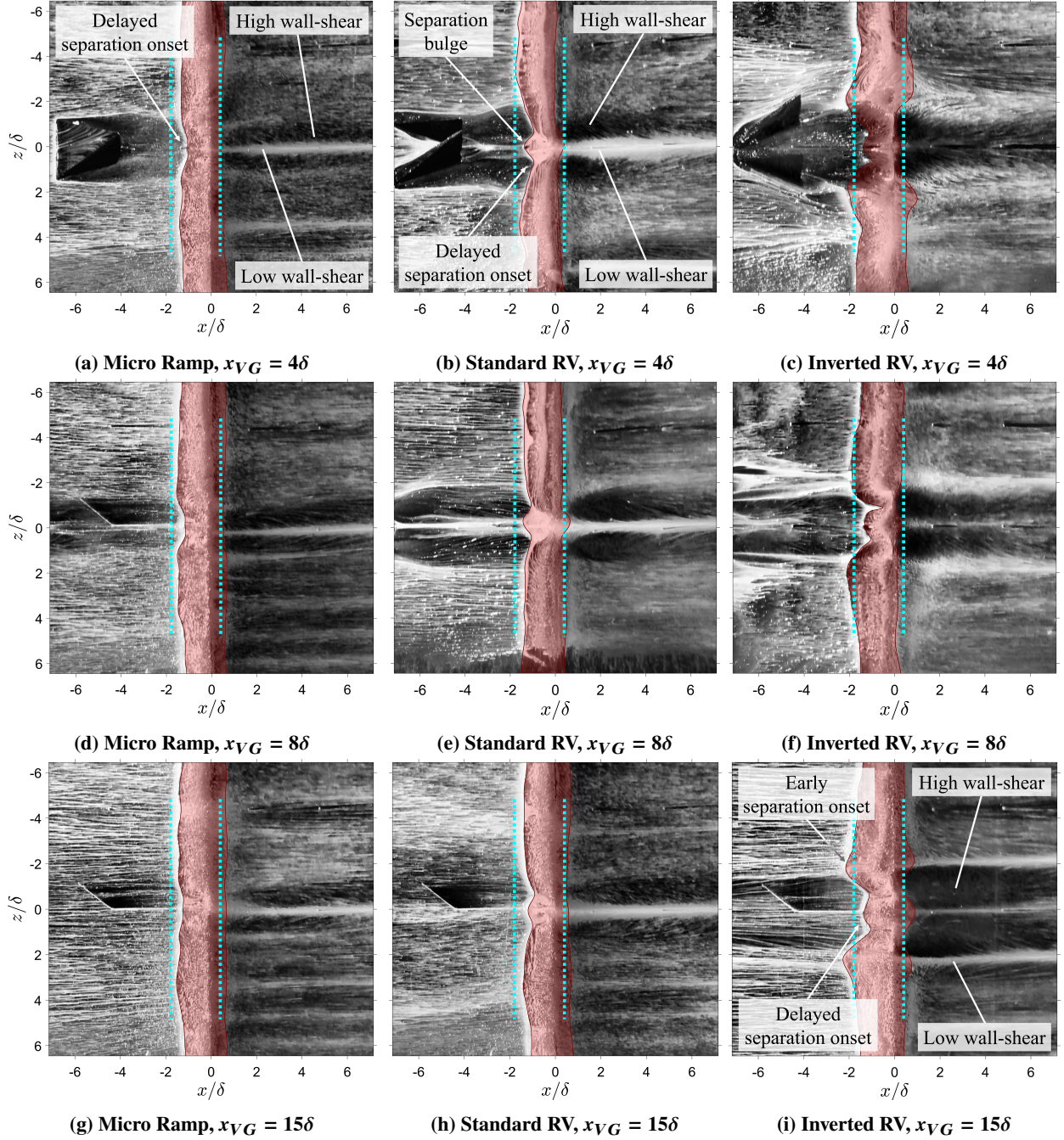


**Fig. 12** Micro ramp, standard ramped-vanes, and inverted ramped-vanes surface streamlines for various upstream device locations.

out while remaining near the surface (Fig. 9), which results in considerable areas of increased separation.

Surface pressure distributions for the various control devices are presented in Fig. 15. These images are also zoomed into the focus area indicated in Fig. 11. In all images, the separation and reattachment pressure rises appear to ripple with the separation and reattachment streamlines observed from the oil-flow. Furthermore, in several cases low-pressure

streaks are observed downstream of reattachment. These streaks are visible for the micro-ramp cases (Fig. 15a, 15d, & 15g), yet are comparatively less well-defined than for the standard (Fig. 15b, 15e, & 15h) and inverted (Fig. 15c, 15f, & 15i) ramped-vane cases. The streaks for the micro-ramp and standard ramped-vanes are most visible when the devices are placed  $4\delta$  from the hinge line and become more diffuse as the devices are placed farther upstream. In contrast, the streaks become more well-defined for the inverted ramped-vanes when the devices are placed  $15\delta$  from the hinge line. It is hypothesized that these streaks are associated with the low-pressure vortex cores impinging on the ramp surface.

Figure 15 also shows that the influence of the micro-ramps and standard ramped-vanes on the SBLI pressure field seems to diminish as the devices are placed farther away from the hinge line. In contrast, the influence of the inverted ramped-vanes slightly increases with distance from the hinge line. When the inverted ramped-vanes are placed far from the interaction, Fig. 15i shows that they cause particularly severe corrugation of the separation and reattachment pressure rises. For this configuration at all three device locations, there is a reattachment pressure rise gap where

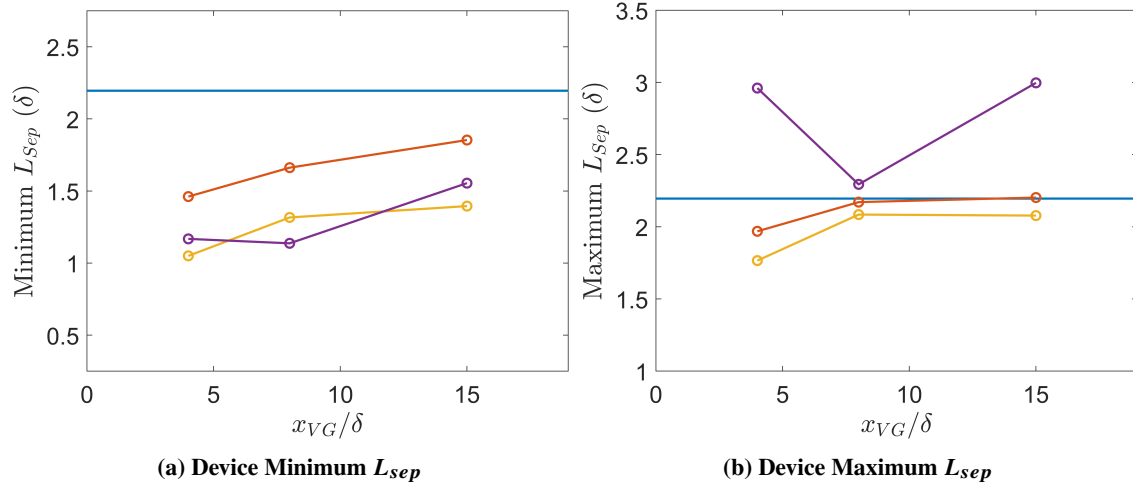


**Fig. 13** Plots of  $L_{sep}$  variation with VG configuration and location. Baseline separation length shown in blue, micro-ramp in red, standard ramped-vane in yellow, and inverted ramped-vane in purple.

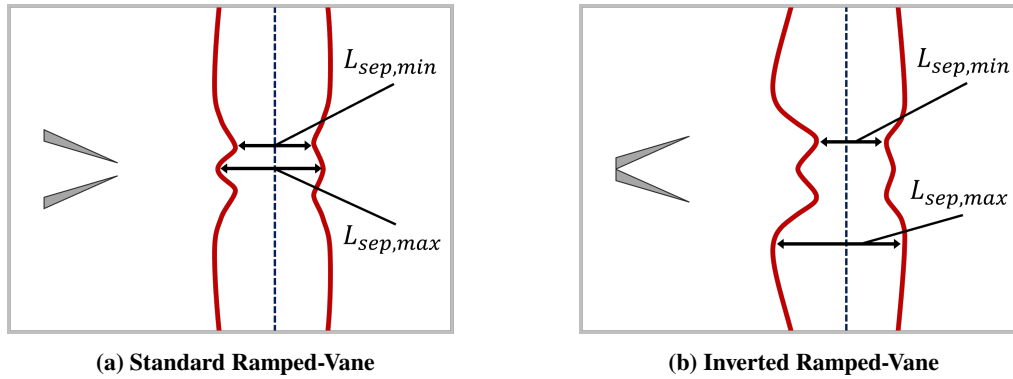


**Fig. 14** Diagrams showing definition of minimum and maximum separation length for typical ramped-vane separation and reattachment streamline structures.



reattachment occurs earlier than in the baseline case. This area is directly downstream of the areas of delayed separation onset. The observed gaps in the separation and reattachment pressure rise are largest when the device is placed  $15\delta$  upstream.

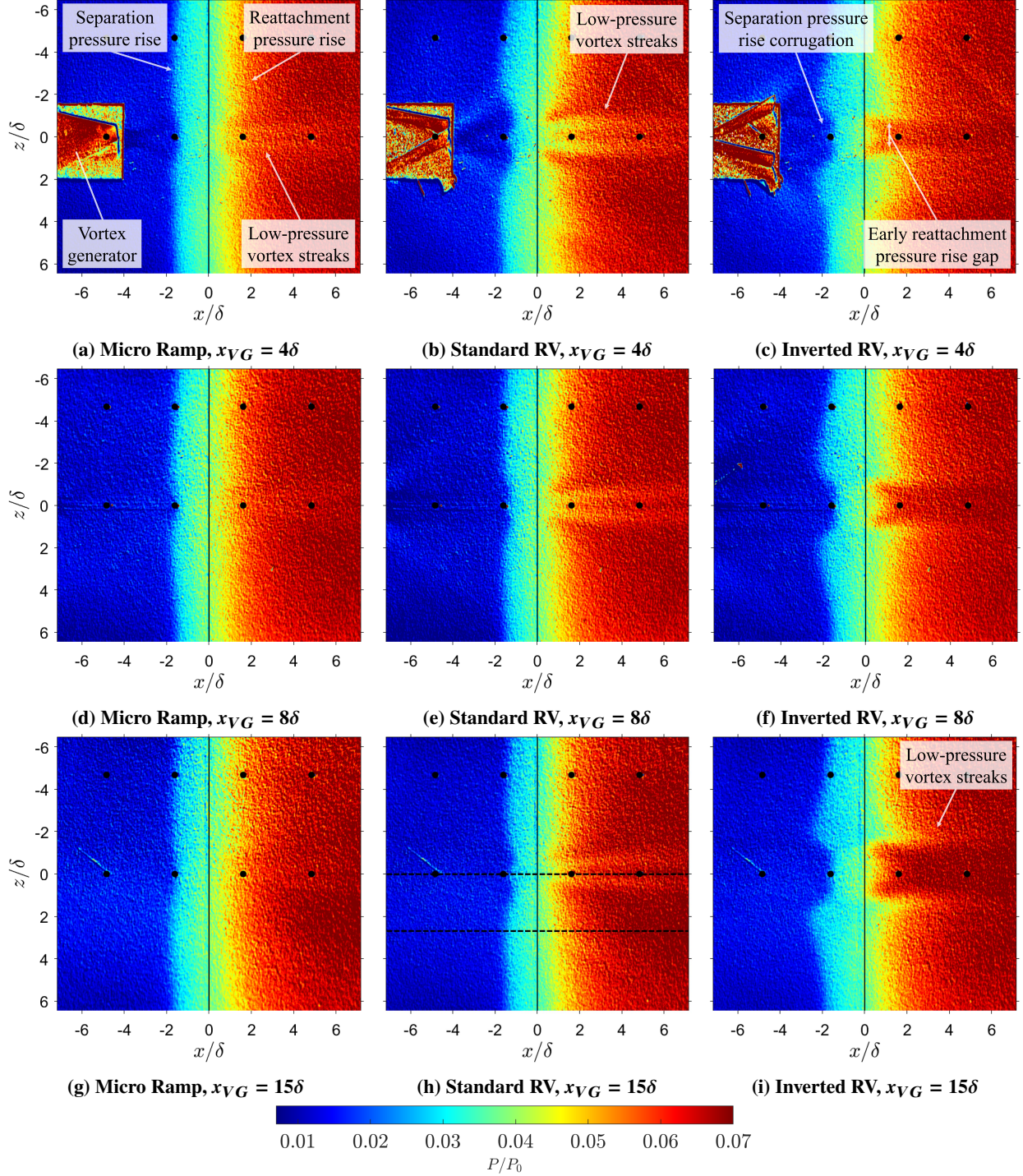


**Fig. 15** Micro-ramp, standard ramped-vane, and inverted ramped-vane pressure fields for various upstream device locations. Black dashed lines indicate Fig. 16 streamwise traverse locations.

Streamwise pressure distributions along the standard ramped vane centerline, as well as  $3\delta$  from the standard ramped vane centerline are compared to the baseline pressure distribution in Fig. 16. The results show that the separation pressure plateaus are approximately the same in all three traces, as predicted by free interaction theory [30]. The centerline flow with standard ramped-vanes experiences the separation pressure rise over a smaller streamwise distance than the baseline case, resulting in a stronger adverse pressure gradient. The relatively lower downstream pressure observed along the standard RV centerline occurs because this trace passes over the streaks believed to be associated with the vortex cores impinging on the ramp surface.

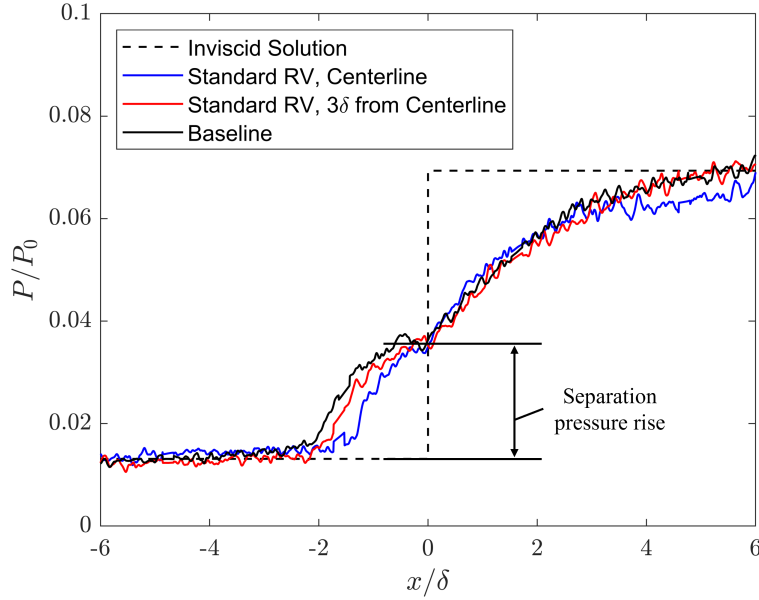
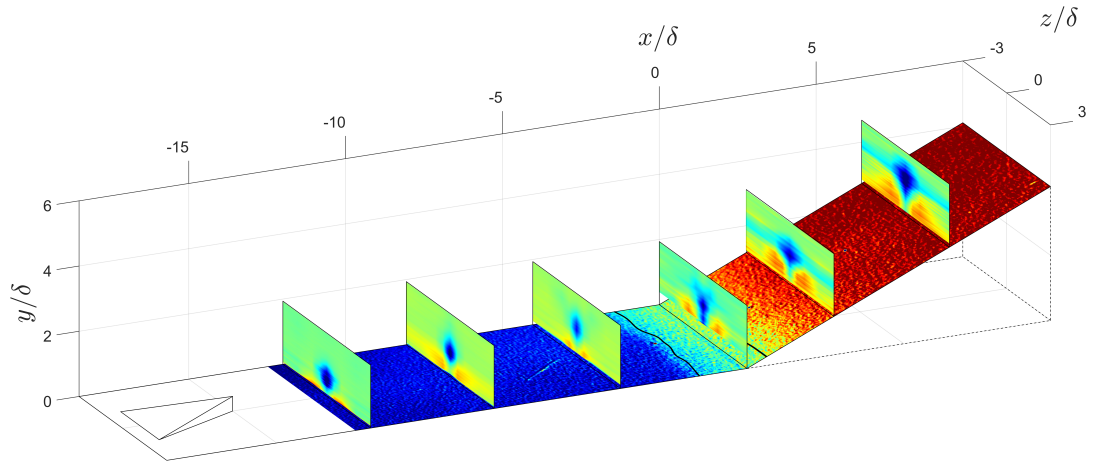


**Fig. 16 Baseline and  $x_{VG} = 15\delta$  standard ramped vane pressure traces.**

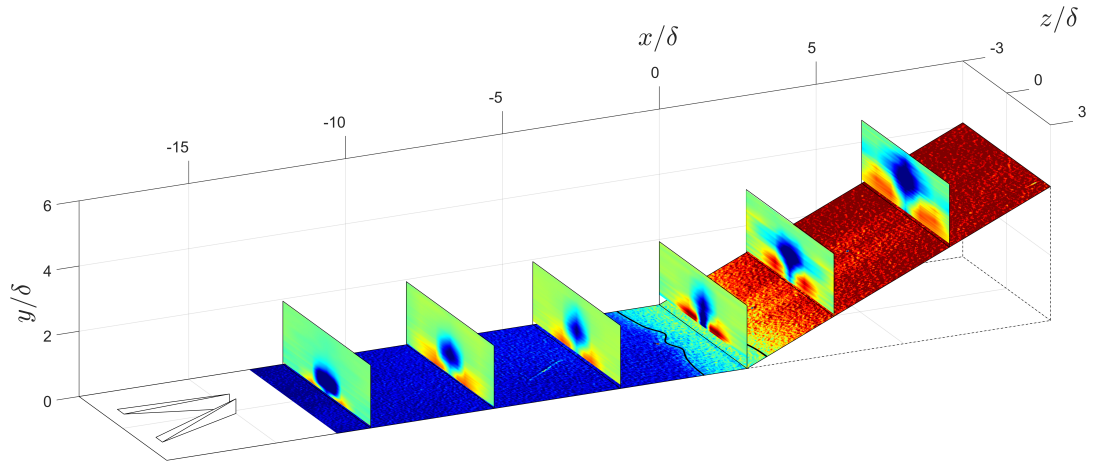
Contour plots of the relative velocity vector magnitude fields for the micro-ramp, standard ramped-vanes, and inverted ramped-vanes positioned  $15\delta$  from the hinge line are presented in Fig. 17. The separation and reattachment locations identified using surface oil-flow visualization as well as the wall pressure field visualizations are overlaid as a reference. Velocity measurements were recorded  $12\delta$ ,  $8\delta$ , and  $4\delta$  upstream of the hinge line, directly along the hinge line, and at streamwise locations  $3\delta$  and  $6\delta$  downstream of the hinge line along the ramp surface.

Figure 17 shows that the boundary between the areas of increased high and low momentum is aligned with the low-pressure streaks visible on the ramp surface. This observation supports the hypothesis that the low-pressure streaks are associated with the vortex cores impinging on the ramp surface. Furthermore, the continued mixing of momentum in the upwash and downwash regions suggests that the vortices are still coherent after passing through the interaction. A similar finding was made by McCormick [31], who showed that vortices induced by ramp-type VGs did not break down and continued to energize the boundary-layer downstream of a Mach 1.58 normal SBLI in a diverging channel flow. However, we note that the return of the VG-induced vortices to the wall may be unique to the geometry of a compression

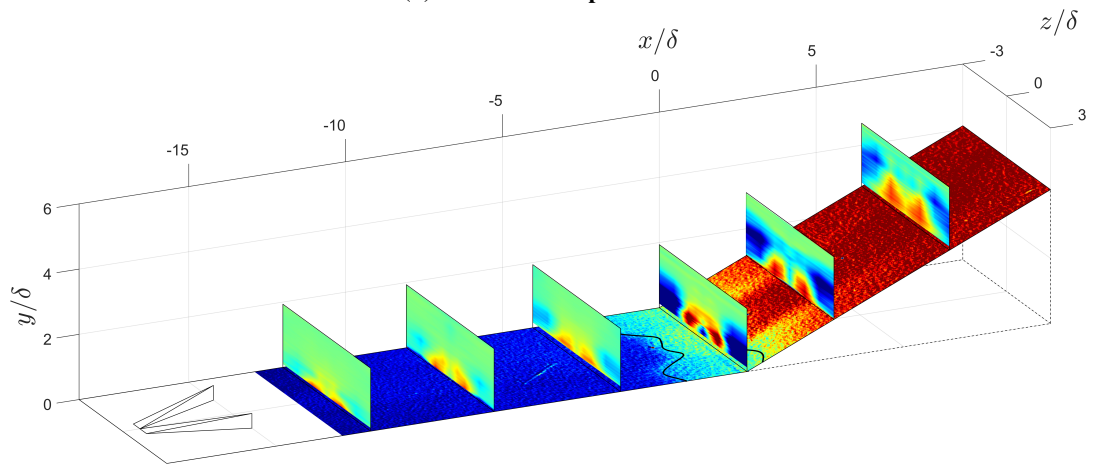




(a) Micro-Ramp



(b) Standard Ramped-Vanes



(c) Inverted Ramped-Vanes

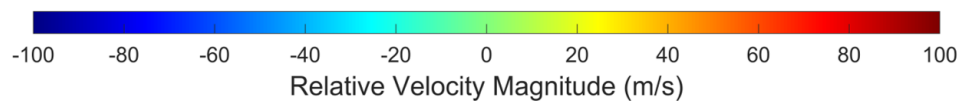


**Fig. 17** VG relative velocity magnitude across compression ramp SBLI at  $x_{VG} = 15\delta$ .

corner, where the VG-induced vortices naturally return to the wall downstream of the hinge line as the wall turns into the flow.

Figure 17 also shows that the SBLI has a significant effect on the VG-induced momentum distribution downstream of the hinge line. In the absence of an SBLI, Fig. 8 suggests that the VG-induced vortices show signs of decay  $11\delta$  downstream of the devices, and that the corresponding regions of streamwise velocity surplus and deficit begin to diminish (Fig. 9). In contrast, Fig. 17 shows that the intensity of relative momentum is larger on the hinge line and ramp surface than that recorded upstream of the SBLI. In particular, the maximum relative velocity at the hinge line of the inverted ramped-vanes (Fig. 17c) is nearly four times that of its maximum upstream value. A similar effect is observed for the maximum velocity deficit. As such, the SBLI appears to exacerbate the effect of the vortices on the momentum distribution.

The introduction of considerable velocity distortion by the VGs downstream of the SBLI is shown schematically for the standard ramped-vanes in Fig. 18. The increased velocity field distortion along the hinge line and ramp surface can be partially explained by the enhanced SBLI three-dimensionality. The regions of near-wall high and low momentum corrugate the separation and cause the shock front to ripple across the span. This behavior, coupled with the coherence of the vortices downstream of reattachment, act as significant perturbative influences that increase spanwise distortion. It is likely that both the vortices and the areas of relative high and low momentum will ultimately be smeared far downstream of the interaction. Importantly, however, this decay may occur over a much larger distance than what would be predicted from observations of the same vortices in the absence of an SBLI.

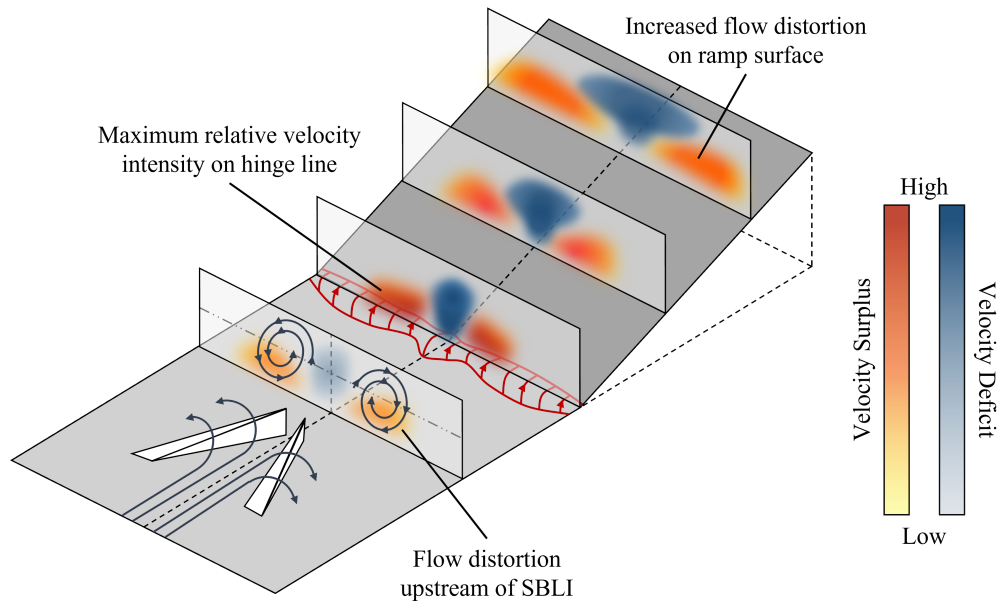


**Fig. 18** Schematic showing increased intensity of relative high and low momentum areas on ramp surface downstream of standard ramped-vane.

In general, Fig. 17 shows that the spanwise segments near the hinge line containing significant near-wall low-momentum demonstrated an increased separation length, while those with additional high-momentum tended to show a decreased separation length. However, it was observed along the standard ramped-vanes centerline that the separation was locally reduced, despite the presence of additional low momentum (see Fig. 17b). It is not immediately obvious why this region did not result in an increased separation length compared to the uncontrolled baseline. One possible reason could be the effect of the VGs not on the mean flow, but on the turbulence. Figure 19 shows that compared to the baseline flow, turbulent fluctuations are increased significantly for standard ramped-vanes along the centerline upstream of the hinge line. Furthermore, the outboard turbulent fluctuation profiles ( $3\delta$  from the device centerline) seem to closely match the baseline profiles. In this spanwise region the separation length with standard ramped-vane control approximately matches that of the baseline flow. Turbulent statistics unfortunately could not be analyzed for the inverted ramped-vanes as too few data points per bin are available to obtain fully converged turbulence quantities in the low-momentum regions on the device shoulders.

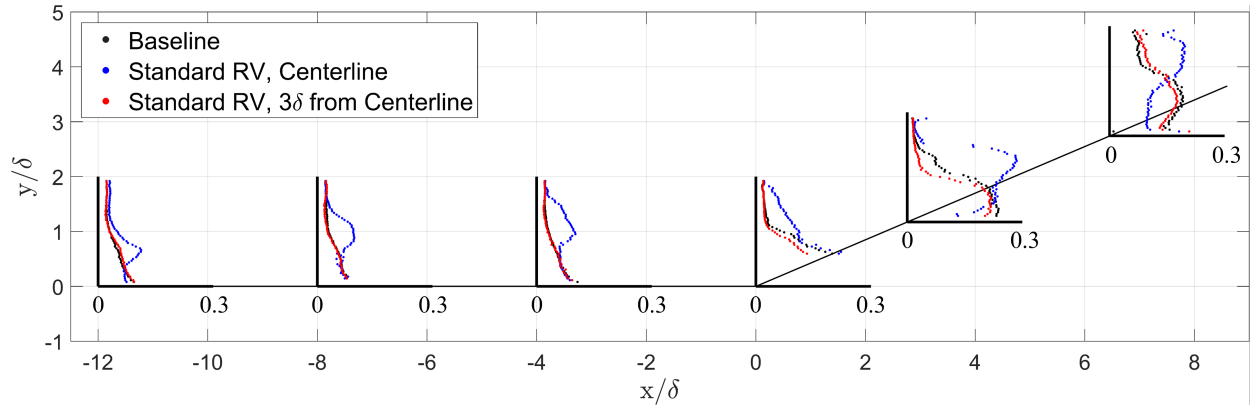


**Fig. 19** Baseline and  $x_{VG} = 15\delta$  standard ramped-vane streamwise turbulent intensity profiles ( $u_{rms}/u_{\infty}$ ) at various locations around the compression ramp hinge line.

#### D. Discussion on the Mechanism of VG Control

Until now, the action of VG control has been described with a focus on the separation process. Namely, VGs are typically thought to mix regions of high and low momentum flow, bringing higher momentum closer to the wall which requires a stronger or more sustained adverse pressure gradient to separate. In turn, the onset of flow separation is delayed, and the size of the separation shrinks. However, it is also worth noting that increasing the near-wall momentum has the negative side-effect that the sonic height is shortened, resulting in reduced upstream pressure communication and a shorter upstream influence length. This leads to a more aggressive adverse pressure gradient and thus promotes separation [1], suggesting that the effects of improved incoming boundary-layer momentum may be relatively minor. In addition, the oil-flow visualization and PSP tests show that the VG-induced vortices generate considerable rippling of the reattachment streamline. This suggests that the action of VG control may not be explained solely through consideration

of the separation mechanism.

It is well known that the compression corner separation and reattachment processes are inherently coupled [18]. The overall pressure rise across the interaction is the sum of the separation and reattachment pressure rises. Free interaction theory suggests that the pressure rise at separation is fixed for a given Mach number [30]. The results (Fig. 16) suggest that this also holds for VG-controlled flows. A constant pressure jump at separation implies that the flow deflection angle at separation ( $\theta_s$ ) is uniform for a given flow field (Mach number and ramp deflection angle). For the flow to reattach, the separated shear layer must gain enough momentum to overcome the pressure rise required at reattachment, allowing the separated shear layer to stagnate on the ramp surface. The necessary shear layer momentum is gained via mixing with the external flow. The reattachment pressure rise is determined by noting that the deflection angle at reattachment is also fixed by the ramp geometry. Consequently, any downstream movement of the separation point must be accompanied by an upstream shift of the reattachment location, and vice versa. This coupling is shown schematically in Fig. 20.

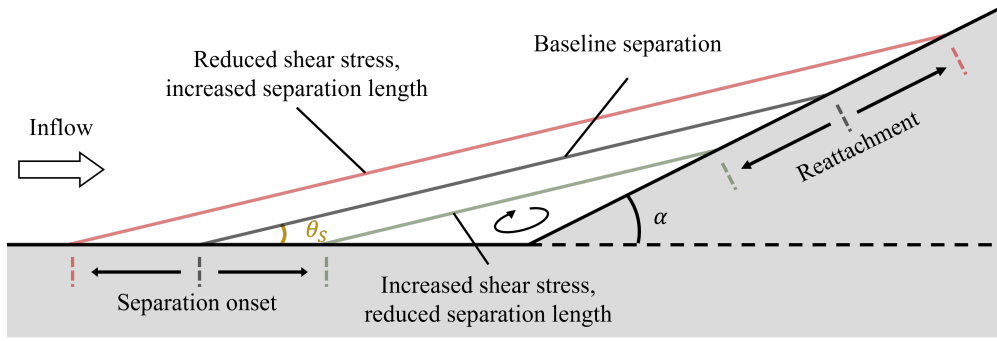


**Fig. 20 Schematic of compression corner flow separation showing coupled movement of separation and reattachment locations.**

Thus, the separated shear layer is shorter in areas where separation is delayed by flow control. Assuming the pressure rise across the interaction is constant (i.e. separations of all lengths must overcome the same pressure rise at reattachment), a shorter separated shear layer needs to gain momentum more quickly. It is likely that this is achieved through enhanced turbulent mixing by the streamwise vortices. The presence of increased turbulent fluctuations in an area of reduced separation relative to the baseline was demonstrated along the standard ramped-vane centerline in Fig. 19. As such, the measurements suggest that the mechanism of VG control may not solely rely on increased near-wall momentum but also on enhanced turbulent mixing within the separated shear layer. Additional experiments are required to prove this interpretation of the VG control mechanism, but are outside the scope of the present investigation.

## V. Conclusions

Experiments have been performed to study VG control of a Mach 3.5, 23° compression corner flow separation. The investigation has yielded the following conclusions:

- 1) All VGs cause the separation to ripple and become more three dimensional, but none remove it altogether. Across three tested placement locations, standard ramped-vanes provide on average an 18% greater separation reduction than micro-ramps in the spanwise areas of maximum effectiveness. Further, for a given device location, standard vane configurations are more effective than inverted vanes at reducing separation. Inverted vanes tend to generate large areas of increased low-momentum near the wall that can locally increase the separation length.
- 2) A VG's optimal location depends on device configuration. Standard vane configurations are more effective when placed near the interaction (around  $4\delta$ ), because the vortices tend to lift off over distance. In contrast, inverted vanes produce a more favorable effect on the separation when placed relatively farther from the interaction (at distances around  $8\delta$ ) because their vortices remain near the floor and spread out with distance. At  $4\delta$  and  $15\delta$ , the areas of increased separation caused by the inverted vanes becomes large.
- 3) The VG-induced vortices remain coherent downstream of the compression corner hinge line. Furthermore, the vortices impinge on the wall downstream of the SBLI, likely as a result of the compression corner geometry. The SBLI causes the VG-induced areas of increased and decreased near-wall momentum to become more intense downstream of reattachment, resulting in significant flow distortion. The consequence of this effect depends on the practical application. The VGs may have a beneficial control effect (or in the case of the inverted vanes, a detrimental control effect) on any subsequent flow separations, but would reduce engine efficiency if the flow distortion progresses directly to the engine face. In the case of a SCRAMjet engine, the increased flow distortion may induce better fuel mixing in the combustion chamber.
- 4) The VGs increase turbulent fluctuations near the wall in areas where there separation length is reduced. It is hypothesized that this result sheds light on the mechanism of VG control, and highlights the role of VGs to enhance mixing in the separated shear layer. Increased mixing causes earlier reattachment, leading to an overall reduction in the length of separation.

Future work in this area is required to definitively establish the mechanism of VG control discussed herein. This may be best handled computationally, where Reynolds stresses and turbulent fluctuations in the area around the flow separation can be identified without the physical limitations of experimental velocimetry techniques.

## Acknowledgments

This work was financially supported by the Winston Churchill Foundation of the United States. The contributions of the technicians Dave Martin, Tony Luckett, and Ciaran Costello are gratefully acknowledged. The support of Tim Missing and Luke Dickinson in the design and operation of experiments is also recognized. The blow-down wind tunnel used in this study is part of the United Kingdom National Wind Tunnel Facility and their support is gratefully acknowledged.

## References

- [1] Babinsky, H., and Harvey, J., *Shock Wave-Boundary-Layer Interactions*, Cambridge Aerospace Series, Cambridge University Press, 2011. <https://doi.org/10.1017/CBO9780511842757>.
- [2] Seddon, J., and Goldsmith, E. L., *Intake aerodynamics*, 2<sup>nd</sup> ed., Blackwell Science, Oxford, 1999.
- [3] Loth, E., Roos, F., Davis, D., Mace, J., Jaiman, R., White, S., and Dutton, C., “Mesoflap and Bleed Flow Control for a Mach 2 Inlet,” *42nd AIAA Aerospace Sciences Meeting and Exhibit*, AIAA Paper 2004-855, 2004. <https://doi.org/10.2514/6.2004-855>.
- [4] Bisek, N. J., Rizzetta, D. P., and Poggie, J., “Plasma Control of a Turbulent Shock Boundary-Layer Interaction,” *AIAA Journal*, Vol. 51, No. 8, 2013, pp. 1789–1804. <https://doi.org/10.2514/1.J052248>.
- [5] Souverein, L., and Debiève, J.-F., “Effect of air jet vortex generators on a shock wave boundary layer interaction,” *Experiments in Fluids*, Vol. 49, 2013, pp. 1053–1064. <https://doi.org/10.1007/s00348-010-0854-8>.
- [6] Titchener, N., and Babinsky, H., “A review of the use of vortex generators for mitigating shock-induced separation,” *Shock Waves*, Vol. 25, 2015. <https://doi.org/10.1007/s00193-015-0551-x>.
- [7] Babinsky, H., Li, Y., and Pitt-Ford, C. W., “Microramp Control of Supersonic Oblique Shock-Wave/Boundary-Layer Interactions,” *AIAA Journal*, Vol. 47, No. 3, 2009, pp. 668–675. <https://doi.org/10.2514/1.38022>.
- [8] Lin, J. C., “Control of turbulent boundary-layer separation using micro-vortex generators,” *30th Fluid Dynamics Conference*, AIAA Paper 1999-3404, 1999. <https://doi.org/10.2514/6.1999-3404>.
- [9] Lin, J. C., “Review of research on low-profile vortex generators to control boundary-layer separation,” *Progress in Aerospace Sciences*, Vol. 38, 2002, pp. 389–420. [https://doi.org/10.1016/S0376-0421\(02\)00010-6](https://doi.org/10.1016/S0376-0421(02)00010-6).
- [10] Bur, R., Coponet, D., and Carpels, Y., “Separation control by vortex generator devices in a transonic channel flow,” *Shock Waves*, Vol. 19, 2009, pp. 521–530. <https://doi.org/10.1007/s00193-009-0234-6>.
- [11] Gartling, D. K., “Tests of Vortex Generators to Prevent Separation of Supersonic Flow in a Compression Corner,” Master’s thesis, The University of Texas at Austin, 1970.
- [12] Barter, J. W., and Dolling, D. S., “Reduction of fluctuating pressure loads in shock/boundary-layer interactions using vortex generators,” *AIAA Journal*, Vol. 33, No. 10, 1995, pp. 1842–1849. <https://doi.org/10.2514/3.12736>.
- [13] Verma, S., Sankar, M., and Raju, C., “Control of shock unsteadiness in shock boundary-layer interaction on a compression corner using mechanical vortex generators,” *Shock Waves*, Vol. 22, 2012. <https://doi.org/10.1007/s00193-012-0369-8>.
- [14] Verma, S. B., and Manisankar, C., “Separation and flow unsteadiness control in a compression corner induced interaction using mechanical vortex generators: Effects of vane size and inter-device spacing,” *Physics of Fluids*, Vol. 34, No. 9, 2022, p. 096105. <https://doi.org/10.1063/5.0106767>.

- [15] Schreyer, A., Sahoo, D., Williams, O. J. H., and Smits, A. J., “Influence of a Microramp Array on a Hypersonic Shock-Wave/Turbulent Boundary-Layer Interaction,” *AIAA Journal*, Vol. 59, No. 6, 2021, pp. 1924–1939. <https://doi.org/10.2514/1.J059925>.
- [16] Lee, S., Loth, E., and Babinsky, H., “Normal shock boundary layer control with various vortex generator geometries,” *Computers & Fluids*, Vol. 49, No. 1, 2011, pp. 233–246. <https://doi.org/10.1016/j.compfluid.2011.06.003>.
- [17] Titchener, N., “An Experimental Investigation of Flow Control for Supersonic Inlets,” Ph.D. thesis, University of Cambridge, Department of Engineering, 2013. <https://doi.org/10.17863/CAM.14077>.
- [18] Souverein, L. J., Bakker, P. G., and Dupont, P., “A scaling analysis for turbulent shock-wave/boundary-layer interactions,” *Journal of Fluid Mechanics*, Vol. 714, 2013, p. 505–535. <https://doi.org/10.1017/jfm.2012.495>.
- [19] Williams, R. D., and Babinsky, H., “Corner effects on the unsteady behaviour of compression corner shock wave/boundary layer interactions,” *AIAA SCITECH 2022 Forum*, AIAA Paper 2022-1181, 2022. <https://doi.org/10.2514/6.2022-1181>.
- [20] Williams, R. D., and Babinsky, H., “Strip theory approach to corner effects in shock-wave boundary layer interactions,” *AIAA SCITECH 2023 Forum*, AIAA Paper 2023-0649, 2023. <https://doi.org/10.2514/6.2023-0649>.
- [21] Anderson, B., Tinapple, J., and Surber, L., “Optimal Control of Shock Wave Turbulent Boundary Layer Interactions Using Micro-Array Actuation,” *3rd AIAA Flow Control Conference*, AIAA Paper 2006-3197, 2006. <https://doi.org/10.2514/6.2006-3197>.
- [22] Lee, S., and Loth, E., “On ramped vanes to control normal shock boundary layer interactions,” *The Aeronautical Journal*, Vol. 122, No. 1256, 2018, p. 1568–1585. <https://doi.org/10.1017/aer.2018.88>.
- [23] Squire, L. C., “The motion of a thin oil sheet under the steady boundary layer on a body,” *Journal of Fluid Mechanics*, Vol. 11, 1961, pp. 161 – 179. <https://doi.org/10.1017/S0022112061000445>.
- [24] Gregory, J. W., Asai, K., Kameda, M., Liu, T., and Sullivan, J. P., “A review of pressure-sensitive paint for high-speed and unsteady aerodynamics,” *Proceedings of the Institution of Mechanical Engineers, Part G: Journal of Aerospace Engineering*, Vol. 222, No. 2, 2008, pp. 249–290. <https://doi.org/10.1243/09544100JAERO243>.
- [25] Colliss, S. P., Babinsky, H., Nübler, K., and Lutz, T., “Vortical Structures on Three-Dimensional Shock Control Bumps,” *AIAA Journal*, Vol. 54, No. 8, 2016, pp. 2338–2350. <https://doi.org/10.2514/1.J054669>.
- [26] Sabnis, K., “Supersonic Corner Flows in Rectangular Channels,” Ph.D. thesis, University of Cambridge, Department of Engineering, 2020. <https://doi.org/10.17863/CAM.59806>.
- [27] Colliss, S. P., “Vortical structures on three-dimensional shock control bumps,” Ph.D. thesis, University of Cambridge, Department of Engineering, 2014.
- [28] Saric, W. S., “Görtler Vortices,” *Annual Review of Fluid Mechanics*, Vol. 26, No. 1, 1994, pp. 379–409. <https://doi.org/10.1146/annurev.fl.26.010194.002115>.

- [29] Nolan, W. R., "A Study of Vortex Generator Behavior," Ph.D. thesis, University of Cambridge, Department of Engineering, 2013.
- [30] Chapman, D. R., Kuehn, D. M., and Larson, H. K., "Investigation of Separated Flows in Supersonic and Subsonic Streams with Emphasis on the Effect of Transition," Tech. Rep. NACA-TR-1356, National Advisory Committee for Aeronautics, 1958.
- [31] McCormick, D. C., "Shock/boundary-layer interaction control with vortex generators and passive cavity," *AIAA Journal*, Vol. 31, No. 1, 1993, pp. 91–96. <https://doi.org/10.2514/3.11323>.